small methods
www.small-methods.com

Realizing Interfacial Electron/Hole Redistribution and Superhydrophilic Surface through Building Heterostructural 2 nm $Co_{0.85}Se$-NiSe Nanograins for Efficient Overall Water Splittings

Fei Ye, Lin Zhang, Chengjie Lu, Zhuoheng Bao, Zeyi Wu, Qiang Liu, Zongping Shao, and Linfeng Hu**

Electrochemical overall water splitting using renewable energy input is highly desirable for large-scale green hydrogen generation, but it is still challenged due to the lack of low-cost, durable, and highly efficient electrocatalysts. Herein, 1D nanowires composed of numerous 2 nm $Co_{0.85}Se$-NiSe nanograin heterojunctions as efficient precious metal-free bifunctional electrocatalyst are reported for both hydrogen evolution reaction (HER) and oxygen evolution reaction (OER) in alkaline solution with the merits of high activity, durability, and low cost. The abundant microinterface among the ultrafine nanograins and the presence of lattice distortion around nanograin interface is found to create a superhydrophilic surface of the electrocatalyst, which significantly facilitate the fast diffusion of electrolytes and the release of the formed H_2 and O_2 from the catalyst surface. Furthermore, synergic effect between $Co_{0.85}Se$ and NiSe grain on adjusting the electronic structure is revealed, which enhances electron mobility for fast electron transport during the HER/OER process. Owing to these merits, the rationally designed $Co_{0.85}Se$-NiSe heterostructures display efficient overall water splitting behavior with a low voltage of 1.54 V at 10 mA cm^{-2} and remarkable long-term durability for the investigated period of 50 h.

1. Introduction

Green hydrogen as produced from renewable energy is a very promising clean energy carrier to address the significant threat of serious environmental pollution, global warming, and energy crisis caused by fossil fuel combustion. Electrocatalytic water splitting, launched by anodic oxygen evolution reaction (OER) and a cathodic hydrogen evolution reaction (HER), has attracted great interest in the past decades because it uses the abundant water as hydrogen source and widely accessible solar or wind power as indirect energy input.[1–3] However, due to the unfavorable thermodynamics and sluggish kinetics of these two half reactions, highly efficient electrocatalysts are always required to reduce the overpotential and accelerate the reaction rate.[4–6] Especially, low-cost, durable bifunctional catalysts for both HER and OER in the same electrolyte with low overpotentials to drive catalysis is highly intriguing owing to their integrated merits in simplifying the device fabrication and reducing the cost.[7–9] Recently, remarkable efforts have been devoted to developing novel, high-performance bifunctional catalysts for overall water splitting based on non-noble transition metals, such as oxides, hydroxides, sulfides, phosphides, and selenides.[10–15] Typically, Wu et al. reported a bifunctional catalyst containing amorphous NiO nanosheets coupled with ultrafine Ni and MoO_3 nanoparticles, affording low overpotentials of 62 mV at 10 mA cm^{-2} and 347 mV at 100 mA cm^{-2} for HER and OER.[10] Park's group developed a bifunctional catalyst comprising $La_{0.5}Sr_{0.5}CoO_{3-\delta}$ and K-$MoSe_2$, which respectively require overpotentials of 128 and 230 mV to deliver 10 mA cm^{-2} for the HER and OER.[16]

Due to the high intrinsic electronic conductivity and favorable activity for water electrochemical splitting, transition metal selenides (Co_xSe, Ni_xSe, $MoSe_2$, WSe_2, etc.) have been paid particular importance because of their high.[14,17–19] Most recently, the construction of heterostructures is an effective strategy to further boost the electrocatalytic performance of transition metal selenides.[20] In general, a heterostructure is defined as the composite structure which couples different

F. Ye, C. J. Lu, Z. H. Bao, Q. Liu, L. F. Hu
School of Materials Science and Engineering
Southeast University
Nanjing 211189, P. R. China
E-mail: linfenghu@seu.edu.cn
L. Zhang, Z. Y. Wu, L. F. Hu
Department of Materials Science
Fudan University
Shanghai 200433, P. R. China
Z. P. Shao
State Key Laboratory of Materials-Oriented Chemical Engineering
College of Chemical Engineering
Nanjing Tech University (NanjingTech)
Nanjing 210009, P. R. China
E-mail: shaozp@njtech.edu.cn
Z. P. Shao
WA School of Mines: Minerals
Energy and Chemical Engineering (WASM-MECE)
Curtin University
Perth, Western Australia 6102, Australia

The ORCID identification number(s) for the author(s) of this article can be found under https://doi.org/10.1002/smtd.202200459.

DOI: 10.1002/smtd.202200459

materials with interfacial interaction. The construction of such heterostructured catalysts not only produce more favorable interfacial sites for the adsorption/activation of active species but also enable electron transfer between different components, which is extremely beneficial for enhancing the electrocatalytic activity.[21,22] On the other hand, recent progress has shown that superhydrophilic surface of electrocatalysts can facilitate the fast release of excessive amounts of as-generated H_2/O_2 bubbles on the electrode surface.[23–26] In principle, when the electrode shows strong adhesion towards H_2/O_2 bubbles during the water splitting, the diffusion of the electrolyte ions would be impeded and the active sites are significantly blocked. It is no double that construction of bifunctional HER/OER heterostructured catalyst with a superhydrophilic surface is very promising for overall water splitting. However, known that wettability is generally determined by the chemical composition and geometrical morphology of the electrode surface,[27] such a consideration is still very challenging and has rarely been realized up to date.

Herein, we report that intrinsic superhydrophilic surface and interface electron structure tuning can be simultaneously realized in ultrafine, 2 nm $Co_{0.85}Se$, NiSe nanograins, which can be facilely through an in situ synergistic selenization strategy for highly efficient overall water splitting. X-ray photoelectron spectroscopy (XPS) characterization identifies the electron redistribution in the $Co_{0.85}Se$-NiSe heterostructures with electron transfer from Co^{2+} in $Co_{0.85}Se$ side to Ni^{2+} in NiSe side. Such a superhydrophilic, heterostructured electrocatalyst delivers a low overpotential of 92 mV for HER and 238 mV for OER at a current density of 10 mA cm^{-2}, respectively. When two identical $Co_{0.85}Se$-NiSe electrodes are used as both the cathode and anode in a two-electrode system, it needs only a cell voltage of 1.54 V to achieve current density of 10 mA cm^{-2} together with a remarkable durability of 50 h. This finding sheds light on the development strategy of high-performance bifunctional OER/HER electrocatalysts from superhydrophilic transition metal selenide heterojunctions.

2. Results and Discussion

2.1. Synthesis and Structural Characterization

In situ synergistic selenization strategy of NiO and 2-methylimidazole cobalt (ZIF-67) on Ni foam (NF) was proposed to grow $Co_{0.85}Se$-NiSe heterostructured nanowire arrays (**Figure 1**a). After etching in HCl (3 M) solution and an aging treatment in deionized (DI) water, X-ray diffraction (XRD) and scanning electron microscope (SEM) characterizations demonstrate the formation of a layer of NiO crumpled nanosheets on NF surface (Figures S1 and S2, Supporting Information), which should be an ideal seed layer for the heterostructural growth of cobalt-rich ZIF-67 nanocrystals. After activation with 2-methylimidazole and a subsequent aging in methanol solution containing of cobalt nitrate and 2-methylimidazole for 24 h, the dark green color of the Ni/NiO substrate changed into purple, confirming the successful growth of ZIF-67 crystals. The enlarged diffraction pattern at 2-theta in the range of 5°–35° well matched that of the crystallized ZIF-67 phase (Figure S3a, Supporting Information). The Fourier transform infrared (Figure S3b, Supporting Information) and Raman (Figure S3c, Supporting Information) spectra further identified the formation of ZIF-67 on the Ni/NiO substrate. SEM and transmission electron microscopy (TEM) observations revealed uniform polyhedron morphology of these as-grown ZIF-67 with a size of about 2 µm (Figure S4, Supporting Information), and the corresponding X-ray energy-dispersive spectroscopy (EDS) elemental mapping verified the uniform distribution of Co, C, and N elements in the framework (Figure S5, Supporting Information). We found that packing density of this ZIF-67 layer is highly dependent on the molar ratio of the cobalt sources. As shown in Figures S6–S8 in the Supporting Information, the coverage ratio of ZIF-67 polyhedrons exhibited a gradual increase until the feeding of $Co(NO_3)_2 \cdot 6H_2O$ reached up to 0.16 M. We consider that the heterogrowth mechanism of ZIF-67 on NiO layer should be ascribed to the as-attached plentiful –OH groups on NiO surface during aging in water, which could interact with ligand 2-methylimidazole to induce the growth of ZIF-67 crystal. However, ZIF-67 was not able to be grown directly on Ni Foam, similar with the phenomenon as reported previously in MOFs@Graphene oxide systems.[28]

After a synergistic selenization by solvothermal treatment of the ZIF-67@NiO/Ni precursor at 180 °C for 4 h, the lavender color of ZIF-4 changed to black, suggesting the phase transformation of some metal selenides. SEM observation (Figures S9–S13, Supporting Information) clearly showed the solvothermal time dependent morphology evolution of ZIF-67@NiO/Ni precursor during the synergistic selenization process. First, vertical pyramid-like nanoarrays with a thickness of ≈200 nm were formed on the Ni foam after a solvothermal reaction for 1 h (Figure S9, Supporting Information). The pyramid-like nanoarray gradually converted into nanosheet arrays with the width of about 300 nm when solvothermal time was up to 2 h, the nanosheet emerged with the width about 300 nm (Figure S10, Supporting Information). Increase of the solvothermal time to 4 h gave rise to nanowire array morphology with lengths of several micrometers, as shown in Figure S11 in the Supporting Information. Nanowires were connected with each other, which can facilitate electronic transport as well as ion transport to the whole active area (Figure S12, Supporting Information). Note that morphology evolution was almost completed at this stage, and the further increase of solvothermal time than 4 h resulted in no apparent morphology changes (Figure S13, Supporting Information). XRD patterns contained two series diffraction peaks of both hexagonal NiSe (Joint Committee on Powder Diffraction Standards (JCPDS) No. 02-0892) and $Co_{0.85}Se$ phase (JCPDS No. 52-1008) (Figure S11a, Supporting Information). In addition, we found that the synergistic selenization of NiO and ZIF-67 was essential for the formation of the uniform sized nanowires owing to the "baffle plate" effect of ZIF-67.[29] The absence of ZIF-67 in this selenization strategy resulted in pure NiSe wires with inhomogeneous width with sizes above 1 µm (NiO-180-4h, Figure S14, Supporting Information). The formation of such a $Co_{0.85}Se$-NiSe nanograin based nanowire is very complicated, and ZIF-67 framework should be completely destroyed during the solvothermal treatment, and recrystallization process occurs which plays a key role on the morphology evolution. Although the reason of this morphology

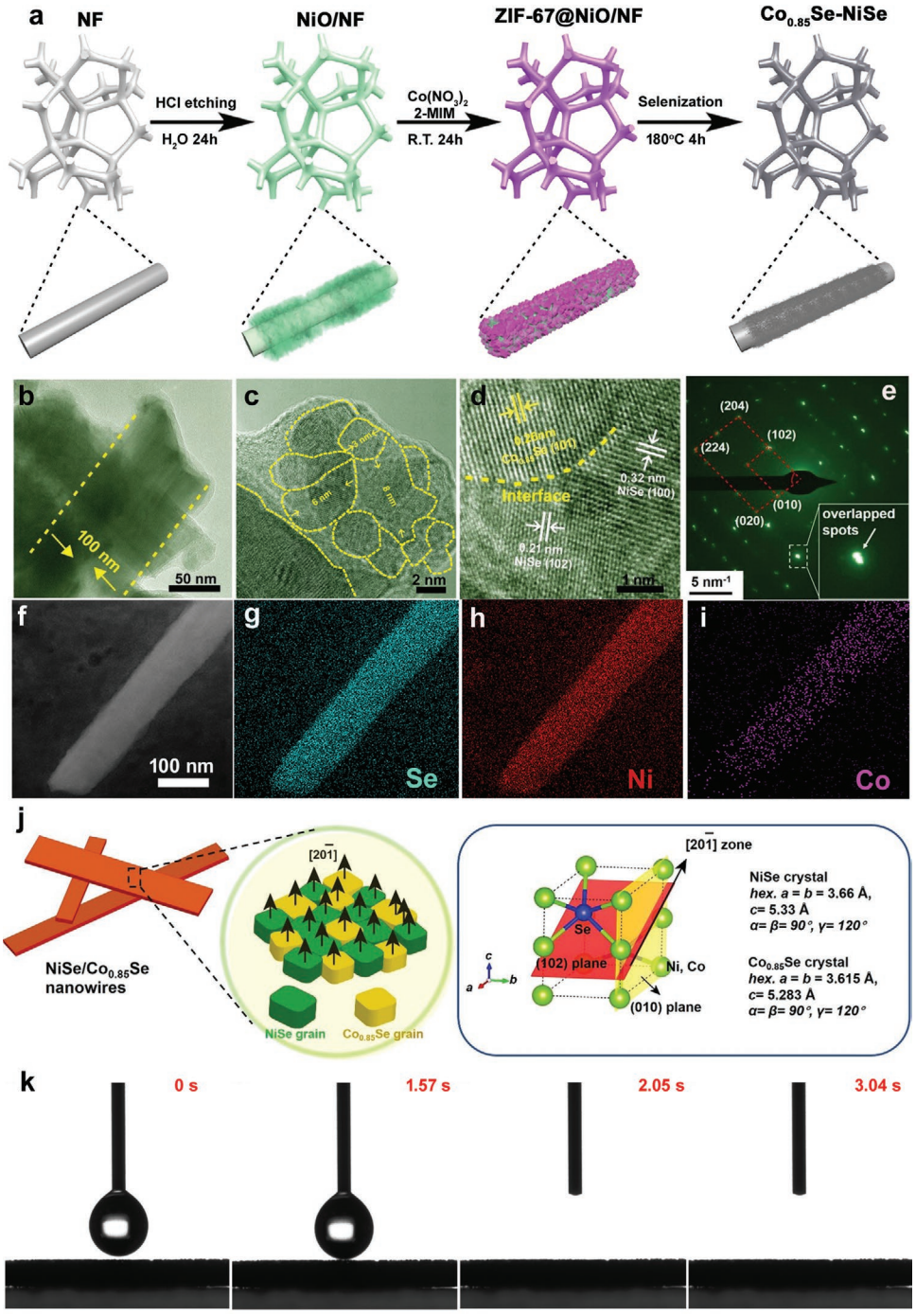

Figure 1. Sample characterization. a) The synthetic route. b–d) Typical TEM and HRTEM images of $Co_{0.85}Se$-NiSe heterojunction nanowire. e) Corresponding SAED pattern and f–i) EDS Elemental mapping of Ni, Co, and Se elements of $Co_{0.85}Se$-NiSe. j) Structural model of NiSe and $Co_{0.85}Se$. k) Water drop contact angles (CA) indicate superhydrophilic properties of $Co_{0.85}Se$-NiSe@Ni.

evolution is still not very clear, we consider the basicity of the solvothermal solution should be responsible. Note that our selenization process was carried out with the addition of NaOH into the solvothermal solution. In the previous work on the formation of $Co_{0.85}Se$ nanowires reported by the other group,[30] similar morphology evolution has also been observed in a basic environment using $CO(NH_2)_2$ as initial reactant.

TEM observation was carried out to reveal the microstructure of the as-formed NiSe/$Co_{0.85}Se$ nanowire arrays. The low-magnification image (Figure 1b) confirmed the uniform nanowire morphology about 100 nm in width. Importantly, the magnified TEM observation demonstrated that each individual nanowire showed a nanoscale nest-like structure with a large number of 2–5 nm packed NiSe and $Co_{0.85}Se$ nanograins (Figure 1c).

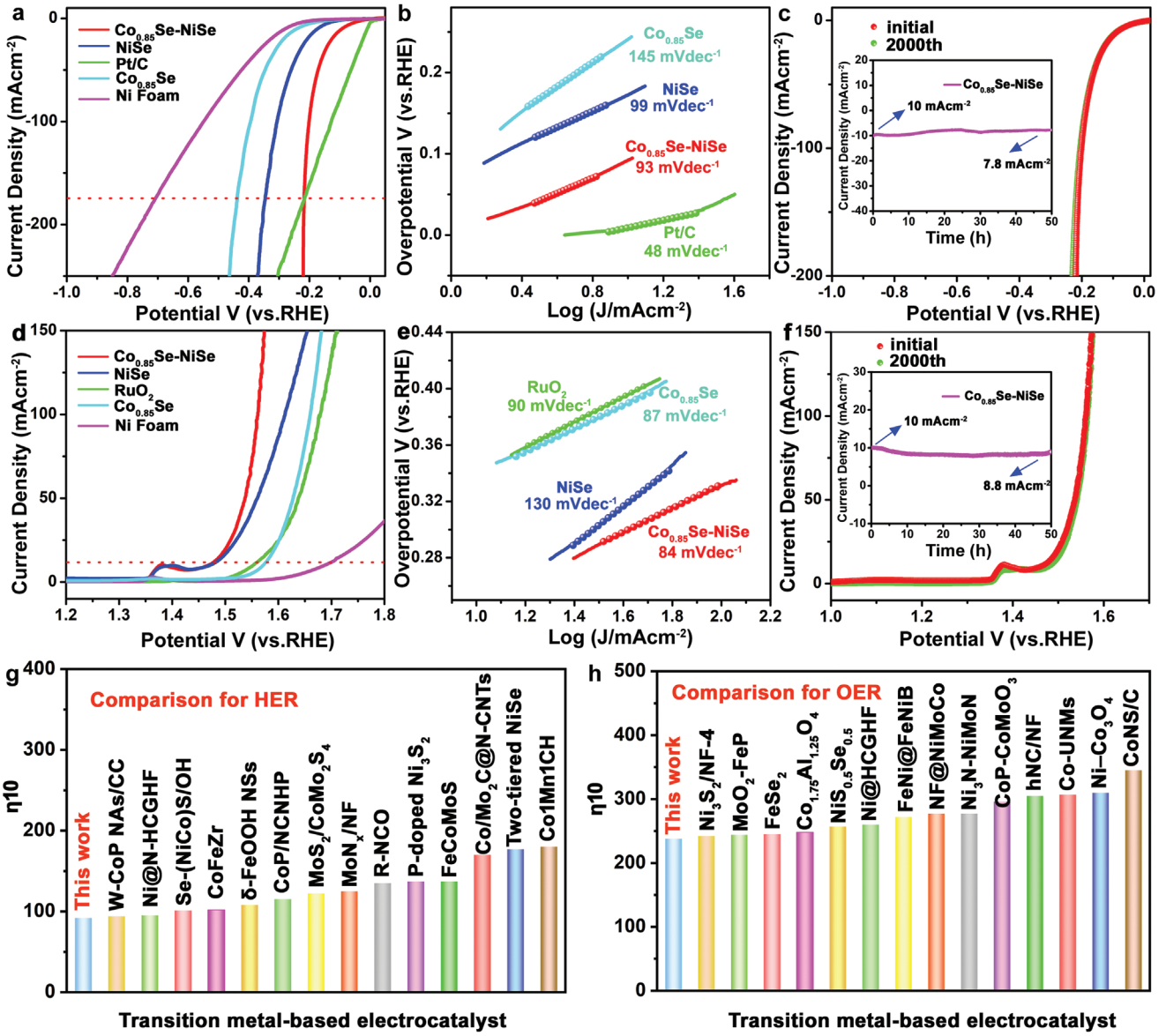

Figure 2. HER/OER performance characterization. a,b) LSV curves with 90% *iR*-corrections and Tafel plots for $Co_{0.85}Se$-NiSe, NiSe, $Co_{0.85}Se$, and Pt/C for the HER. c) Polarization curves for $Co_{0.85}Se$-NiSe before and after 2000 cycles for HER. Inset: *I–t* curve for $Co_{0.85}Se$-NiSe at the η10 for 50 h. d–f) LSV curves with 90% *iR*-corrections and Tafel plots for $Co_{0.85}Se$-NiSe, NiSe, $Co_{0.85}Se$, and Pt/C for the OER. Polarization curves for $Co_{0.85}Se$-NiSe before and after 2000 cycles for OER. Inset: *I–t* curve for $Co_{0.85}Se$-NiSe at the η10 for 50 h. g–h) Comparison of η10 with reported transition metal-based electrocatalysts.

In the high-resolution TEM (HRTEM) image (Figure 1d), the lattice fringes of 0.21, 0.32 nm correspond well to the (102), (100) crystal plane of hexagonal NiSe crystal. The as-observed 0.26 nm lattice fringe from an adjacent nanograin well matched the spacing of $Co_{0.85}Se$ (101) plane. The grain boundary of the NiSe and $Co_{0.85}Se$ nanograins can be easily distinguished under TEM observation, indicating the formation of a great deal of NiSe/$Co_{0.85}Se$ heterojunctions inside an individual nanowire. The selected area electron diffraction (SAED) in Figure 1e taken from an individual wire further identified the coexistence of NiSe and $Co_{0.85}Se$ phase. The SAED pattern along the [20$\bar{1}$] zone shows sharp diffraction spots, suggesting the single-crystal nature of each nanowire. The X-ray EDS elemental mapping of an individual $Co_{0.85}Se$-NiSe nanowire confirms all components (Ni, Co, and Se) were distributed uniformly with the nanowire (Figure 1f–i). Note that magnified view of the diffraction spots in **Figure 2**d were elongated along a constant *d*-spacing. Since $Co_{0.85}Se$ crystal exhibited similar crystallographic arrangement to NiSe crystal with slightly smaller lattice parameters (Figure 1j), we consider this unique SAED pattern should be attributed to the overlap of the diffraction from both NiSe and $Co_{0.85}Se$ nanograins. Accordingly, it is rational that each nanowire is a mosaic structure composed of the closely packed NiSe and $Co_{0.85}Se$ nanograins with the same [20$\bar{1}$] orientation. For comparison, the TEM observation of pure NiSe nanowires grown as the same method without the Co sources was also

carried out. The corresponding HRTEM image and bright diffraction spots in SAED pattern demonstrate the highly crystalline nature and the absence of any grain-interface inside the wire (Figure S15, Supporting Information).

Interestingly, we detected quite different surface wettability between the as-grown NiSe/$Co_{0.85}Se$ heterostructures and pure NiSe nanowire arrays (Figure 1k and Figure S16, Supporting Information). It was observed that the electrolyte (1 M KOH) drop could penetrate deeply into the $Co_{0.85}$Se-NiSe@Ni sample with a contact angle of 0° after 2.04 s, demonstrating a superhydrophilic surface. Such a surface would significantly facilitate the contact between electrocatalysts and electrolyte, thereby facilitating the fast release of excessive amounts of as-generated H_2/O_2 bubbles on the electrode surface.[31] In contrast, the pure NiSe@Ni sample exhibited a hydrophobic surface with a much higher contact angle of 134.38° after 5.99 s. Note that the aforementioned HRTEM results revealed much denser grain-boundaries in $Co_{0.85}$Se-NiSe nanowire than that in pure NiSe nanowire. Accordingly, we infer that the as-observed superhydrophilicity of $Co_{0.85}$Se-NiSe nanowire arrays should be related to the abundant interface inside the nanowires, which has been confirmed by density functional theory (DFT) calculations (see in Section 2.3).

2.2. Electrocatalytic Performance

Benefiting from the merits as-mentioned above, the $Co_{0.85}$Se-NiSe@Ni electrode should be very promising for the electrocatalytic applications. HER performance of the superhydrophilic $Co_{0.85}$Se-NiSe@Ni sample was then evaluated in a 1.0 M KOH electrolyte with a typical three-electrode system. Figure 2a shows the polarization curves of the samples with 90% IR compensation. Commercial 20% Pt/C was also tested for comparison. The optimized $Co_{0.85}$-NiSe/NF catalyst shows enhanced catalytic activity at a current density of 10 and 200 mA cm^{-2} with overpotentials of 92 mV (η10) and 219 mV (η200), respectively, which are lower than those required for the $Co_{0.85}$Se, NiSe, and NF counterparts (Table S2, Supporting Information). Notably, the activity of $Co_{0.85}$Se-NiSe catalyst at a large current density exceeds that of Pt/C/NF and most non-noble metal-based catalysts (Figure 2g and Table S3, Supporting Information). A series of tests showed that the initial Co concentration was also important for yielding an optimized catalyst for the HER (Figure S17, Supporting Information). The excellent activity of $Co_{0.85}$Se-NiSe can be ascribed to the favorable H* adsorption kinetics on the heterointerface.[32,33] The Tafel slope of $Co_{0.85}$Se-NiSe is 93 mV dec^{-1}, which is smaller than that of $Co_{0.85}$Se (145 mV dec^{-1}) and NiSe (99 mV dec^{-1}), demonstrating more rapid reaction kinetics of $Co_{0.85}$Se-NiSe (Figure 2b). Such a Tafel slope suggests that the HER route of $Co_{0.85}$Se-NiSe follows the Volmer–Heyrovsky mechanism.[34] The exchange current density (j_0) value is highly dependent on the nature of the catalyst and indicates the intrinsic electron transfer rate between the catalyst and the electrolyte.[35] As shown in Figure S18 in the Supporting Information, the exchange current density for $Co_{0.85}$Se-NiSe is 1.13 mA cm^{-2}, which is larger than that of $Co_{0.85}$Se (0.18 mA cm^{-2}) and NiSe (0.23 mA cm^{-2}). Additionally, the electrochemical double layer capacitance (C_{dl}) of an electrocatalyst is proportional to its electrochemically active surface area (ECSA).[36] The C_{dl} of $Co_{0.85}$Se-NiSe, NiSe, and $Co_{0.85}$Se are 20.0, 15.9, and 5.7 mF cm^{-2}, respectively (Figures S19, Supporting Information). Such a high C_{dl} value suggests that the nanowire-structured $Co_{0.85}$Se-NiSe sample affords more exposed active sites, thus leading to enhanced catalytic efficiency. The turnover frequency (TOF) value for $Co_{0.85}$Se-NiSe is 0.24 s^{-1} per site at 100 mV in 1.0 M KOH (Figure S20, Supporting Information), which is larger than that of NiSe sample (0.035 s^{-1}). The high TOF value of $Co_{0.85}$Se-NiSe sample is in well agreement with its excellent activity toward the HER. Apart from the catalytic activity, the long-term durability is another important factor for the electrocatalyst.[37] The working electrode was handled for 2000 cycles using a continuous cyclic voltammetry (CV) measurement between 0 and –0.4 V (vs reversible hydrogen electrode (RHE)). As shown in Figure 2c, the polarization curves of $Co_{0.85}$Se-NiSe catalyst before and after 2000 CV test nearly overlapped with each other, especially at the low overpotential region. After continuous HER CV scanning of 2000 cycles in 1 M KOH, the polarization curve of $Co_{0.85}$Se-NiSe catalyst shows about 11 mV decrease on overpotential at 200 mA cm^{-2}. In addition, the *I–t* test suggested that the current density maintained almost 78% during 50 h test. The results confirm that $Co_{0.85}$Se-NiSe catalyst possessed superior stability in a long-term electrochemical process in alkaline. The excellent HER performance in the alkaline system means that the catalyst can easily cooperate with most non-noble metal OER catalysts, which usually shows good activity in alkaline medium, for the effective electrocatalytic water splitting.

The OER performance of the $Co_{0.85}$Se-NiSe@Ni catalyst was also evaluated in 1 M KOH (Figure S21, Supporting Information). Meanwhile, a commercial RuO_2 catalyst was used as a benchmark. The OER polarization curves of different samples are shown in Figure 2d. Similar trend to that of HER activity was observed in the OER activity of $Co_{0.85}$Se-NiSe composites. As exhibited in Figure 2d and Table S4 in the Supporting Information, the $Co_{0.85}$Se-NiSe catalyst showed the lowest overpotential of 270 mV to achieve a current density of 20 mA cm^{-2}, which is remarkably lower than that of pure $Co_{0.85}$Se@Ni (363 mV) and NiSe@Ni (279 mV), respectively. It is noteworthy that our $Co_{0.85}$Se-NiSe heterostructured sample (η_{10} and η_{100} of 238 and 331 mV, respectively) outperforms commercial RuO_2@NF, especially at relatively high current densities. As shown in Figure 2e, the Tafel slope of $Co_{0.85}$Se-NiSe heterostructure is 84 mV dec^{-1}, smaller than those of $Co_{0.85}$Se (87 mV dec^{-1}), NiSe (130 mV dec^{-1}) and RuO_2 (90 mV dec^{-1}), demonstrating the kinetic merit of $Co_{0.85}$Se-NiSe for water oxidation. The OER activity of $Co_{0.85}$Se-NiSe heterostructures also surpasses that of many other reported nonprecious metal OER catalysts in alkaline solution, as shown in Figure 2h and Table S5 in the Supporting Information. In addition, the ECSA results further indicate that $Co_{0.85}$Se-NiSe sample owned relatively higher active area, which is 6.1 times and 1.3 times larger than that of $Co_{0.85}$Se@Ni, NiSe@Ni, respectively (Figure S20, Supporting Information). The TOF value for $Co_{0.85}$Se-NiSe at 350 mV was estimated to 0.42 s^{-1} in alkaline media (Figure S22, Supporting Information), which is larger than that of NiSe (0.18 s^{-1}). Moreover, the $Co_{0.85}$-NiSe catalyst also showed excellent stability by

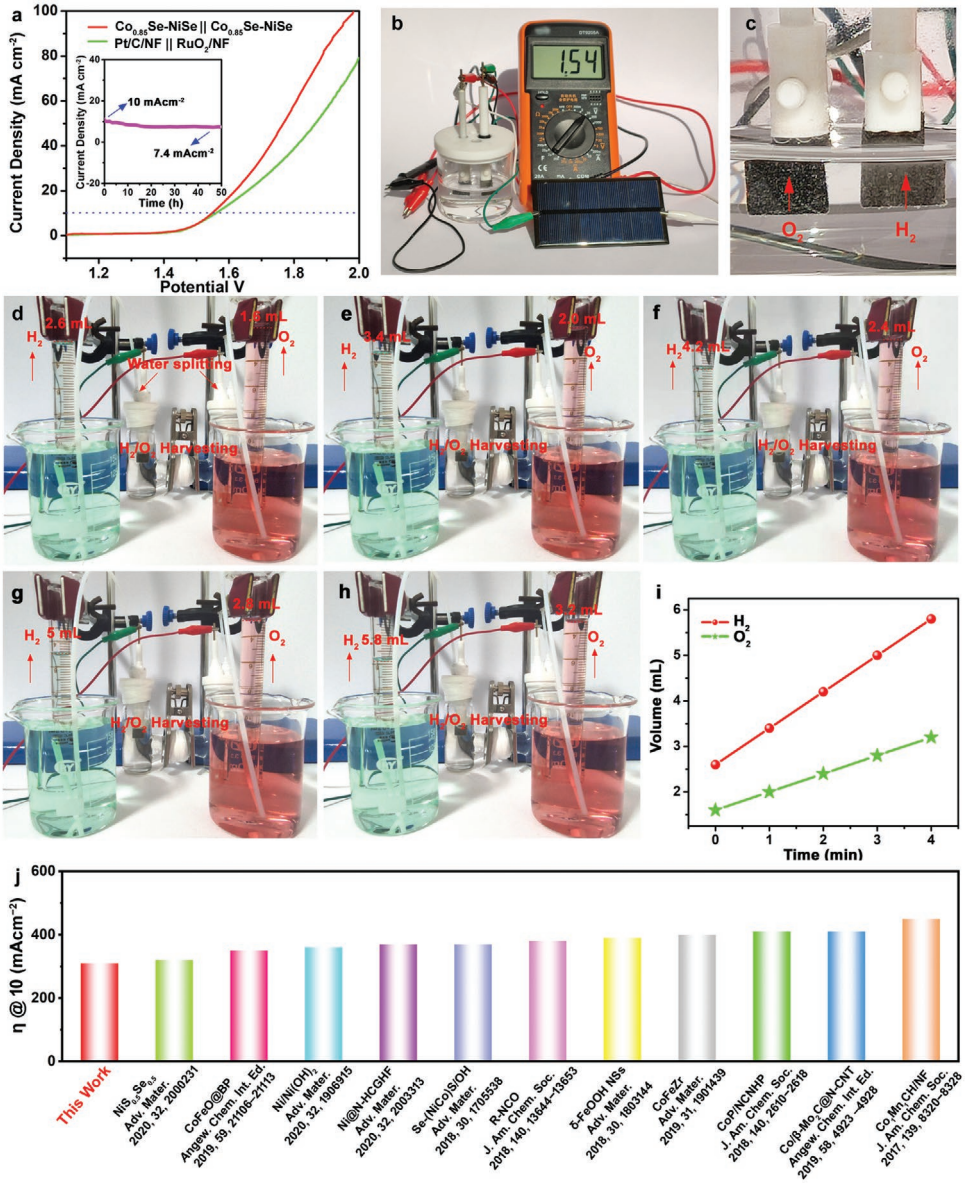

Figure 3. Overall water splitting performance. a) Polarization curves for $Co_{0.85}Se$-NiSe || $Co_{0.85}Se$-NiSe and Pt/C/NF || RuO_2/NF for overall water splitting in 1 M KOH (two-electrode structure). Inset: Chronoamperometry curve of $Co_{0.85}Se$-NiSe || $Co_{0.85}Se$-NiSe recorded at an overpotential of 310 mV. b,c) Photograph of a water-splitting device driven by a solar cell (ca. 1.54 V) and photograph showing the generation of O_2 and H_2 bubbles on the surface of $Co_{0.85}Se$-NiSe. d–h) Gas collection device of water splitting in 1.0 M KOH aqueous solution at 0, 1, 2, 3, and 4 min, respectively. i) Amount of H_2/O_2. Time-dependent experimentally measured versus time for $Co_{0.85}Se$-NiSe in 1.0 M KOH aqueous solution. j) Comparison with state-of-the-art overall water splitting electrocatalysts.

the nearly overlapped polarization curves before and after the 2000 CV cycles. The chronoamperometric curve inserted in Figure 2f further confirms the negligible degradation after 50 h operation. SEM observation of our $Co_{0.85}Se$-NiSe sample after 2000 HER/OER CVs cycling (Figure S23, Supporting Information) indicates that our sample well remained the initial nanowire morphology without drastic aggregation, ensuring efficient mass transfer, large number of active sites and as-observed high stability. linear sweep voltammograms (LSV) and electrochemical impedance spectroscopy (EIS) curves showed that the initial Co concentration was also important for yielding an optimized catalyst for the OER, which had a similar trend to HER (Figure S24, Supporting Information). We also optimized the solvothermal time of 4 h to further enhance the electrocatalytic activity (Figures S25 and S26, Supporting Information).

To explore the potential for practical applications, a water splitting electrolysis cell was then assembled by employing the bifunctional $Co_{0.85}Se$-NiSe@Ni electrode as both the anode and cathode. As illustrated in **Figure 3**a, the $Co_{0.85}Se$-NiSe || $Co_{0.85}Se$-NiSe device exhibited typical overall water splitting behavior with a cell voltage of 1.54 V to achieve a current density of 10 mA cm^{-2}. Such a performance is superior

to that of Pt/C/NF || RuO_2/NF (1.56 V). Equally attractively, the $Co_{0.85}Se$-NiSe || $Co_{0.85}Se$-NiSe cell displays a long-term stability with 74% retain in activity after 50 h of continuous operation at 1.54 V (Inset in Figure 3a). To confirm the potential application of solar water electrolysis, we constructed a solar-to-hydrogen system to realize economic and sustainable H_2 production. As shown in Figure 3b, the multimeter indicates that the solar panel generates a voltage of 1.54 V under sunlight. The generation of gas bubbles could be clearly observed at the surface of both the anode and cathode when powered by the solar panel (Figure 3c). Such a solar power assisted water splitting device makes it possible to convert low-voltage electricity into chemical energy. The nearly 100% Faradic yield toward full water splitting of $Co_{0.85}Se$-NiSe by the water drainage method. The gas-collection device of water splitting constructed in the lab as shown Figure 3d–h and Figure S27 (enlarged images) in the Supporting Information further identifies the volume ratio of H_2 to O_2 is about 2:1 (Figure 3j). Remarkably, the water splitting performances of our $Co_{0.85}Se$-NiSe heterojunction sample surpassed that of most high-performance electrocatalysts reported previously and recently (Figure 3j), such as $NiS_{0.5}Se_{0.5}$ (η10 = 320 mV),[38] CoFeO@Black Phosphorus (η10 = 350 mV),[39] Ni/Ni(OH)$_2$ (η10 = 360 mV),[40] Ni@N-HCGHF (η10 = 320 mV),[41] Se-(NiCo)S/OH (η10 = 370 mV),[42] R-NCO (η10 = 380 mV),[43] δ-FeOOH NSs (η10 = 390 mV),[44] CoFeZr (η10 = 400 mV),[45] CoP/NCNHP (η10 = 410 mV),[46] Co/β-Mo_2C@N-doped carbon nanotube (η10 = 410 mV),[47] and Co_1Mn_1CH/NF (η10 = 450 mV).[48]

2.3. Mechanism Study

XPS characterization was performed to clarify the merits of our heterojunction design in the HER/OER process. The corresponding XPS survey spectrum shows the presence of Co, Ni, Se, O, N, and C elements in the nanowire array sample (**Figure 4**a). With regard to Ni $2p_{3/2}$ region, the main peak can be deconvoluted into three subpeaks of Ni-Se (852.3 eV), Ni-O (855.4 eV), and satellite peaks (860.2 eV), respectively (Figure 4b).[49] The Co $2p_{3/2}$ spectrum in Figure 4c delivers four doublets, which can be ascribed to the Co—Co bond (778.0 eV), Co—Se bond (781.8 eV), Co—O bond (785.9 eV) owing to the surface oxidation, and satellite peaks, respectively.[50] Compared to the pure NiSe counterpart (NiO-180-4h), the binding energies of Ni 2p in our $Co_{0.85}Se$-NiSe heterojunctions negatively shift to 0.6 eV. By contrast, positive shift of 0.8 eV for Co $2p_{3/2}$ peak has also been observed

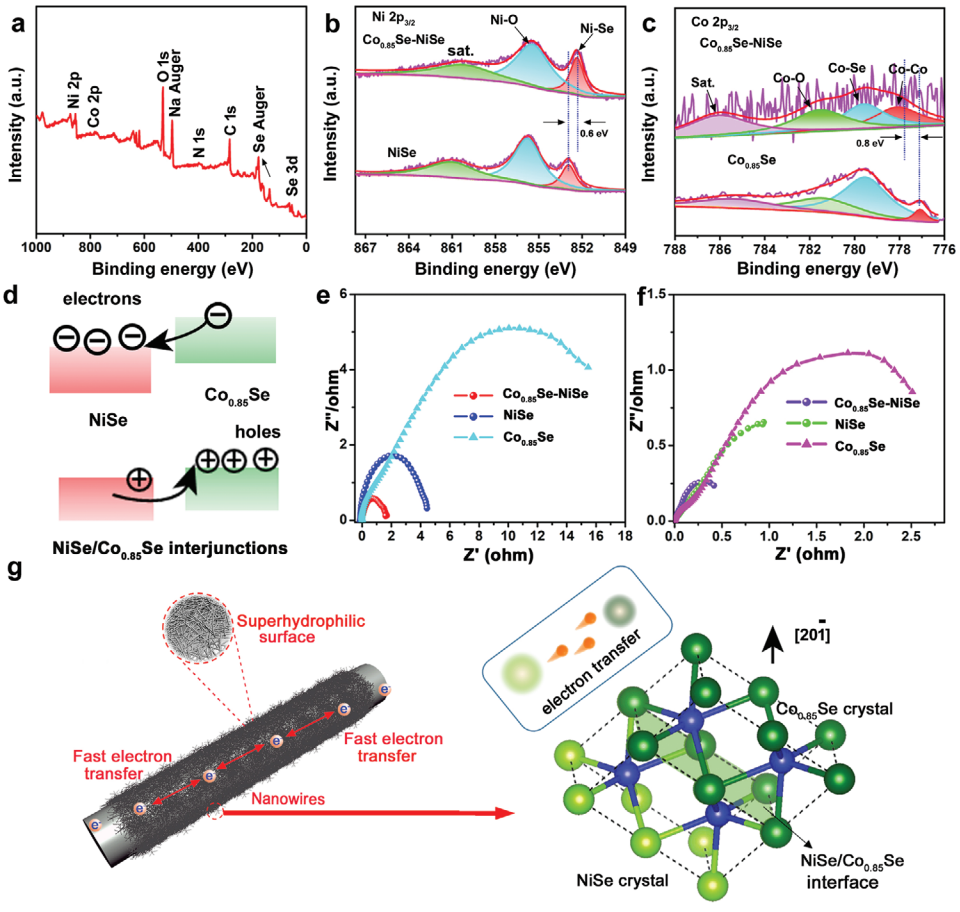

Figure 4. Charge transfer mechanism. a) Wide scan spectra of the $Co_{0.85}Se$-NiSe heterostructure. b,c) Ni $2p_{3/2}$ and Co $2p_{3/2}$ XPS for NiSe and $Co_{0.85}Se$-NiSe. d) Electrons transfer of NiSe/$Co_{0.85}Se$ interjunctions. e,f) EIS curves of $Co_{0.85}Se$-NiSe, NiSe, $Co_{0.85}Se$ composites for HER and OER. g) Schematic illustration of the water splitting activity enhancing mechanism of the $Co_{0.85}Se$-NiSe heterostructure in alkaline media.

in $Co_{0.85}Se$-NiSe sample compared to pure $Co_{0.85}Se$ counterpart, which was prepared by calcining ZIF-67 and selenium powder directly. These results indicate the electron redistribution in the $Co_{0.85}Se$-NiSe heterojunction with electron transfer from Co^{2+} in $Co_{0.85}Se$ to Ni^{2+} in NiSe, resulting in the electron accumulation on NiSe side and hole accumulation on $Co_{0.85}Se$ side of the heterojunction (illustrated in Figure 4d).[51] This interfacial electron redistribution plays an important role in regulating the catalytic ability. In general, the electron accumulation on NiSe side will be beneficial to the occurrence of the HER because the HER needs to trap electrons to generate H_2, while the hole accumulation on $Co_{0.85}Se$ side facilitates the OER because the hole is usually the active site for the oxidation reaction.[52] The regulated electronic structure in our $Co_{0.85}Se$-NiSe heterojunction was further confirmed by impedance spectroscopy in Figure 4e,f, which delivered the smallest charge transfer resistance (R_{ct}) for $Co_{0.85}Se$-NiSe heterojunction in this series including $Co_{0.85}Se$, NiSe and $Co_{0.85}Se$-NiSe. The decreased R_{ct} suggests superior electrical conductivity of $Co_{0.85}Se$-NiSe during catalyzing HER/OER.

To get a deeper understanding on the electrocatalytic mechanism of the $Co_{0.85}Se$-NiSe heterojunctions, the samples after the HER, OER, and stability test were studied by XRD and XPS characterizations. As shown the XRD pattern in Figure S28a,c in the Supporting Information, the diffraction peaks of the samples after the HER and stability test are similar to those of the pristine $Co_{0.85}Se$-NiSe sample other than a slightly decreased peak intensity, indicating the absence of phase evolution during HER.[53] XPS characterizations of the sample after long-term HER process was carried out to identify the chemical composition of the postreaction catalyst. No apparent changes of Ni, Co, Se, and O XPS spectrum (Figures S29 and S30, Supporting Information) have been detected in the pristine $Co_{0.85}Se$-NiSe sample and the catalyst after the 2000 CVs HER operation, demonstrating the outstanding HER stability for long-time application. However, compared with the HER process, the OER process is more complex. XRD pattern (Figure S24b, Supporting Information) shows the peak intensity of the $Co_{0.85}Se$-NiSe after the OER disappeared after the 2000 CVs OER process (Figure S28d, Supporting Information). This result demonstrates the possible phase evolution accompanied with the loss of crystalline nature. XPS analysis further clarifies this conclusion (Figures S29 and S30, Supporting Information). The Ni $2p_{3/2}$ and Co $2p_{3/2}$ peaks of the sample after the OER delivered three pairs of peaks. The peaks intensity corresponding to Ni and Co atoms reduced, while the peaks intensity ascribed to Ni(Co)-O increased. In addition, from the O 1s XPS spectrum in Figure S29 in the Supporting Information, the convolutional area of –OH group peak significantly increased during the OER process, indicating the possible generation of metal (oxy) hydroxides.[54–56] The intensity of Se 3d peak gradually reduced during the long term OER process and no distinct peaks in the Se 3d spectrum after the stability test, indicating the Se species dissolution during the reaction[57,58]

Finally, DFT simulation was conducted to provide further insights of the superhydrophilic origin and electrocatalytic merits of our $Co_{0.85}Se$-NiSe heterojunctions. After the geometry optimization, it can be seen that the $Co_{0.85}Se$ and NiSe grains share the same space group with similar lattice parameters. Interestingly, the obvious lattice distortion occurs on the $Co_{0.85}Se$-NiSe interface of heterojunctions, which could be attributed to the displacement of Se atoms towards the crystal surface (**Figure 5**a). Accordingly, both Co and Ni atoms on surface exhibit a larger electron exchange range than those in bulk sample (Figure 5b), and the corresponding adsorption energies of –O and –OH functional groups on Co/Ni cation atoms of $Co_{0.85}Se$-NiSe heterojunction are remarkably higher than those of unitary $Co_{0.85}Se$ and NiSe (Figure 5c), leading to the increased number of –OH groups on the $Co_{0.85}Se$-NiSe sample surface. In principle, abundant hydroxyl groups on the surface are favorable for the adsorption of dissociative water and results in a superhydrophilic property.[59] Therefore, it is rational that the superhydrophilic nature of the $Co_{0.85}Se$-NiSe heterojunction should be originated from the enhanced –OH adsorption energy.

Moreover, the reason of the improved HER performance of $Co_{0.85}Se$-NiSe heterojunction is also revealed by DFT simulation. Generally, unitary $Co_{0.85}Se$ or NiSe exhibits rather poor HER performance. In fact, in the simulation of H^+ adsorption process on the surface Co or Ni atoms in unitary $Co_{0.85}Se$ or NiSe, the value of adsorption energy is unable to be achieved, which could be assigned to the electrostatic repulsion between H^+ and study object. This result is well consistent with the actual case. In contrast, the $Co_{0.85}Se$-NiSe heterojunction delivers a significantly enhanced H^+ adsorption energy of 2.53 eV on the Se atoms in the distorted lattice, which suggests the favorable tendency of HER occurrence on the catalyst surface. On the other hand, DFT calculations have been carried out to clarify the origin of enhanced OER performance of $Co_{0.85}Se$-NiSe heterojunction. Since it is still difficult to clearly identify the reaction mechanism in terms of the local coordination structure and the electronic structure of active centers during the long-term OER cycles, we preliminarily used the initial crystal $Co_{0.85}Se$-NiSe structure in this theoretical simulation, which is similar to some previous works reported by other groups.[52,60] Figure 5d depicts the simulated three-step OER process to conduct the activation free energy calculations of $Co_{0.85}Se$-NiSe heterojunction during the OER process. As shown in Figure 5e, for the unitary NiSe catalyst, Step 2 serves as the potential determining step of the OER process, which exhibits the transformation from *OH to *O (the asterisk denotes an active site on the catalyst surface), and the corresponding activation free energy ($\Delta G^{\ddagger}$) barrier of is 0.66 eV. After the $Co_{0.85}Se$-NiSe heterojunction is taken into consideration, the corresponding activation free energy barrier declines to 0.47 eV without altering the potential determining step, which indicates that the formation of *O is favorable on the heterojunction surface. Besides, similar result could be found in the case of OER process on Co site in $Co_{0.85}Se$. Step 3 relating with the transformation from *O to *OOH serving as the potential determining step of the OER process, the corresponding energy barrier reduces from 0.79 eV for $Co_{0.85}Se$ to 0.53 eV for $Co_{0.85}Se$-NiSe heterojunction. Overall, the theoretical simulation reveals that the superhydrophilic heterojunction extremely enhances the surface adsorption of hydrophilic –OH functional groups and reduce reaction barriers, thus resulting in superior bifunctional catalytic activity.

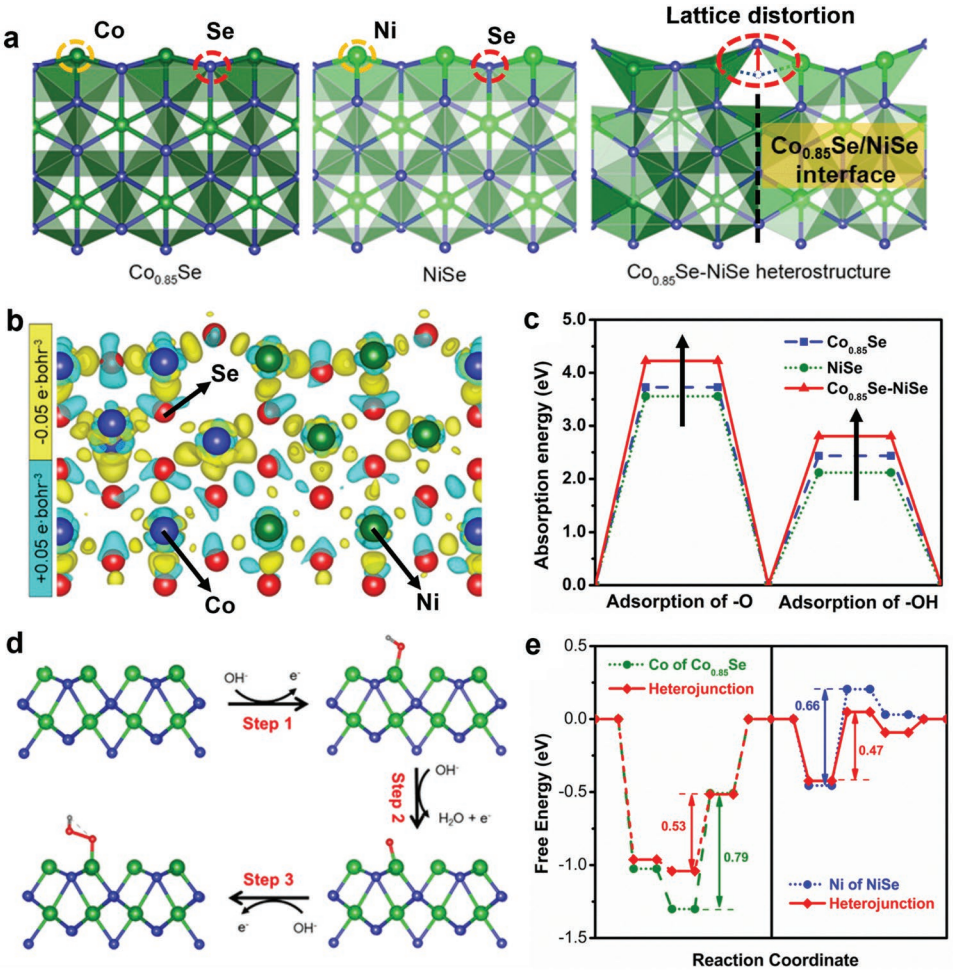

Figure 5. Super-hydrophilic and OER mechanism. a) Schematic diagrams of optimized crystal structure of $Co_{0.85}Se$, NiSe, and $Co_{0.85}Se$-NiSe heterostructure. b) Electron difference density of the $Co_{0.85}Se$-NiSe heterojunction. c) Adsorption energy of –O/–OH functional groups on Co/Ni cation atoms in corresponding samples. d,e) Simulation of the three-step oxygen evolution reaction, with the corresponding free energies.

3. Conclusions

In summary, we have developed an in situ synergistic selenization strategy of NiO and ZIF-67 on Ni foam to grow $Co_{0.85}Se$-NiSe hetertostructured nanowires with intrinsic superhydrophilicity. The $Co_{0.85}Se$-NiSe hetertostructured catalyst achieved a current density of 10 mA cm^{-2} at low overpotential of 92 mV for HER and 238 mV for OER with outstanding stability. It needs only a cell voltage of 1.54 V to achieve 10 mA cm^{-2} when two identical $Co_{0.85}Se$-NiSe heterostructures were used as both the cathode and anode in a two-electrode electrolyzer and it can be easily driven by a 1.54 V solar panel. Such a hetertostructured design brings two main advantages to improve the HER/OER performance: 1) in situ growth of $Co_{0.85}Se$-NiSe heterojunction on Ni Foam with a large number of heterointerfaces are beneficial for adjusting the electronic structure to accelerate electron transport during the HER/OER process (Figure 4g) and 2) the intrinsic superhydrophilic surface gives rise to fast diffusion of electrolytes and the release of the formed H_2 and O_2 from the catalyst surface. Our work provides fundamental insights on electron/hole redistribution through heterostructure interface and sheds light on the development of other catalytic system such as photocatalytic water splitting and CO_2 reduction.

4. Experimental Section

Materials: Cobalt nitrate hexahydrate ($Co(NO_3)_2{\cdot}6H_2O$), 2-methylimidazole ($C_4H_6N_2$), hydrochloric acid, selenium powder, KOH, NaOH, hydrazine monohydrate ($N_2H_4{\cdot}H_2O$, 85 wt%), *N*,*N*-dimethylformamide (DMF, C_3H_7NO, ≥99.8%), methanol anhydrous (CH_3OH, ≥99.5 wt%), and ethanol (C_2H_5OH) were purchased from Sinopharm Chemical Reagent Co., Ltd. RuO_2 was purchased from Alfa Aesar. Ni Foam and Pt/C was purchased from Shanghai Hesen Electric Co., Ltd. There were no further purification of the reagents and solvents. Deionized water was used in the experiments.

Preparation of the NiO/Ni Foam: The NiO nanosheets were prepared by a room-temperature etching growth approach.[61] Briefly, a piece of commercial Ni Foam (3 cm × 3 cm) was cleaned by ethanol and DI water with the assistance of ultrasonication for 15 min each. Then, the clean NF was immersed in HCl (3 M) for 1.5 h to etch the surface, followed by an aging treatment in DI water for 24 h to grow NiO nanosheets on the surface. Finally drying in the air naturally, NiO/NF was successfully obtained.

Preparation of the ZIF-67@NiO/Ni Foam: An in situ crystallization of ZIF-67 on the surface of NiO nanosheet was carried out by the following procedure. NiO/Ni Foam was first activated by 2-methylimidazole

(H-MeIM). Typically, H-MeIM (19.2 mmol) was dissolved in methanol to form a solution with a total volume of 30 mL. The above prepared NiO on Ni substrate was immersed in this solution at 25 °C for 2 h and then 30 mL $Co(NO_3)_2{\cdot}6H_2O$ (4.8 mmol) solution was quickly poured into the above solution. The reaction was performed for 24 h at room temperature. Subsequently it was washed with ethanol and DI water thoroughly. The obtained product was named ZIF-4. By modifying the mass of $Co(NO_3)_2{\cdot}6H_2O$ to 2.4 and 1.2 mmol, ZIF-2 and ZIF-1 were obtained, respectively.

Preparation of the $Co_{0.85}Se$-NiSe Nanowires: The as-prepared Ni foam coated with ZIF-67@NiO was submerged into another 45 mL autoclave containing Se (3.75 mmol, 296 mg), NaOH (7.5 mmol, 300 mg), hydrazine (0.14 mL), and dimethylformamide (DMF) (25 mL). After keeping at 180 °C for 4 h, $Co_{0.85}$Se-NiSe was obtained, which was denoted ZIF-4-180-4h. ZIF-4 was also solvothermal at 180 °C for 1 and 2 h. The samples were named ZIF-4-180-1h and ZIF-4-180-2h, respectively.

Preparation of the $Co_{0.85}Se$: The obtained ZIF-67 and Se powder with a mass ratio of 1:1 were put in two separate positions of a porcelain boat. Then the porcelain boat was put into a furnace with Se powder at the upstream side of the furnace and heated at 600 °C for 3 h under a Ar atmosphere. After cooling to room temperature, $Co_{0.85}Se$ was obtained.[62]

Materials Characterization: Powder XRD analysis was performed on a Bruker D8 Advance diffractometer with Cu-K_a radiation $\lambda = 0.15406$ nm. Raman spectra were collected on a Renishaw in via spectrometer with an excitation laser wavelength of 457.9 nm. X-ray photoelectron spectra (XPS, PHI 5000C electron spectroscopy for chemical analysis system XPS using an Mg K_α) was performed to obtain the elemental composition and chemical state of the materials. The morphologies of as-obtained products were observed by SEM (Hitachi S-4800 electron microscopy). TEM and HRTEM were performed on a JEM-2100F Field Emission Electron microscope, respectively. Fourier transform infrared spectrum was measured from a NICOLETIS10 spectrometer. Contact angles were obtained by a drop shape analyzer (DCAT-11) with 2 µL 1 M KOH solution for each testing.

Electrochemical Measurement: All electrochemical measurements were carried out on the electrochemical workstation (CHI 760 E) in 1 M KOH (pH = 13.8). The as-prepared materials ($Co_{0.85}$Se-NiSe anchored on NF (1 × 1.5 cm), catalyst loading: ≈1.5 mg cm^{-2}), a graphite rod, and Hg/HgO electrode were used as the working electrode, the counter electrode, and the reference electrode, respectively. Before the electrochemical measurements, the electrolyte was purged with N_2 for 1 h to remove the dissolved gases completely. All the potentials were quoted with respect to the RHE through $E_{RHE} = E_{HgO/Hg} + 0.059 \times pH + 0.095$ V.[48] CV was conducted at a scan rate of 100 mV s^{-1} to activate the catalysts. The LSV curves were collected at a sweep rate of 1 mV s^{-1} with 90% IR compensation. The resulting polarization curves were iR-compensated according to the equation

$$E_c = E_m - iR_s \quad (1)$$

where E_c is the corrected potential, E_m is the measured potential experimentally, and R_s is the resistance of the ohmic resistance arising from the electrolyte/contact resistance of the setup and measured by EIS. Long-term stability tests were carried out by using chronoamperometry measurement method. EIS was performed by applying an AC voltage with 5 mV amplitude at the overpotentials of 350 mV for OER and 110 mV for HER from 0.1 Hz to 100 kHz in 1 M KOH electrolyte. Cyclic voltammetry was conducted to probe the double-layer capacitor (C_{dl}) to calculate the ECSA, and the scan rates were 20–200 mV s^{-1}. TOF, denoted the number of molecules transformed at each active site per unit time and a catalytic site being active for HER/OER, is calculated according to the equation as follows

$$TOF = \frac{j}{(n \times Q_e \times N_s)} \quad (2)$$

where j is the HER/OER current (A), n is the number of electrons transferred per hydrogen/oxygen molecule at the electrode (n = 2 or 4), Q_e is the charge of an electron (1.6×10^{-19} C), and N_s is the number of active atoms. The amount of H_2/O_2 generated in the H-type electrolytic cell was collected by the water drainage method. The above tests were all performed at room temperature (25 °C). In overall water splitting tests, the $Co_{0.85}$Se-NiSe nanowires were used as anode and cathode respectively in a two-electrode reactor for overall water splitting. And the RuO_2 and Pt/C were also used as anode and cathode respectively in a two-electrode reactor for overall water splitting. The loadings of RuO_2 and Pt/C on the Ni foam were about 1.5 mg cm^{-2}.

DFT Simulation: The first principle calculations were performed in the framework of DFT as implemented in the Vienna ab initio simulation package. The projector augmented wave method together with the generalized gradient approximation constructed by Perdew–Burke–Ernzerhof for the exchange-correlation energy function was adopted herein. For a precise geometry optimization, the cutoff energy is set to be 500 eV in this work, together with a dense k-grid mesh with a total number of 50. Finally, the convergence criterion for the electronic self-consistent iteration was set to be 10^{-4} eV and the atomic positions were fully relaxed until the force on each atom is less than 0.01 eV Å^{-1}.

Supporting Information

Supporting Information is available from the Wiley Online Library or from the author.

Acknowledgements

This work was financially supported by the National Natural Science Foundation of China (51872051 and 52171203), the Natural Science Foundation of Jiangsu Province (Grants No. BK20211516), the State Key Laboratory of New Ceramic and Fine Processing Tsinghua University (No. KF202102), and the Fundamental Research Funds for the Central Universities (2242022R10090).

Conflict of Interest

The authors declare no conflict of interest.

Data Availability Statement

The data that support the findings of this study are available from the corresponding author upon reasonable request.

Keywords

bifunctional electrocatalysts, charge transfer, $Co_{0.85}$Se-NiSe nanograins, superhydrophilicity, water splitting

Received: April 11, 2022
Revised: April 23, 2022
Published online: May 19, 2022

[1] N. K. Oh, C. Kim, J. Lee, O. Kwon, Y. Choi, G. Y. Jung, H. Y. Lim, S. K. Kwak, G. Kim, H. Park, *Nat. Commun.* **2020**, *11*, 4066.
[2] L. Li, B. Wang, G. W. Zhang, G. Yang, T. Yang, S. Yang, S. C. Yang, *Adv. Energy Mater.* **2020**, *10*, 2001600.
[3] J. Zhang, Q. Y. Zhang, X. L. Feng, *Adv. Mater.* **2019**, *31*, 1808167.
[4] Y. Yang, H. Q. Yao, Z. H. Yu, S. M. Islam, H. Y. He, M. W. Yuan, Y. H. Yue, K. Xu, W. C. Hao, G. B. Sun, H. F. Li, S. L. Ma, P. Zapol, M. G. Kanatzidis, *J. Am. Chem. Soc.* **2019**, *141*, 10417.

[5] Q. Z. Qian, J. H. Zhang, J. M. Li, Y. P. Li, X. Jin, Y. Zhu, Y. Liu, Z. Y. Li, A. E. Harairy, C. Xiao, G. Q. Zhang, Y. Xie, *Angew. Chem., Int. Ed.* **2021**, *60*, 2.
[6] B. H. R. Suryanto, Y. Wang, R. K. Hocking, W. Adamson, C. Zhao, *Nat. Commun.* **2019**, *10*, 5599.
[7] G. R. Cai, W. Zhang, L. Jiao, S. H. Yu, H. L. Jiang, *Chem* **2017**, *2*, 791.
[8] F. Yu, H. Q. Zhou, Y. F. Huang, J. Y. Sun, F. Qin, J. M. Bao, W. A. Goddard, S. Chen, Z. F. Ren, *Nat. Commun.* **2018**, *9*, 2551.
[9] Z. R. Zhang, C. Feng, C. X. Liu, M. Zuo, L. Qin, X. P. Yan, Y. L. Xing, H. L. Li, R. Si, S. M. Zhou, J. Zeng, *Nat. Commun.* **2020**, *11*, 1215.
[10] X. P. Li, Y. Wang, J. J. Wang, Y. M. Da, J. F. Zhang, L. L. Li, C. Zhong, Y. D. Deng, X. P. Han, W. B. Hu, *Adv. Mater.* **2020**, *32*, 2003414.
[11] Y. Jia, L. Z. Zhang, G. P. Gao, H. Chen, B. Wang, J. Z. Zhou, M. T. Soo, M. Hong, X. C. Yan, G. R. Qian, J. Zou, A. J. Du, X. D. Yao, *Adv. Mater.* **2017**, *29*, 1700017.
[12] J. Gautam, Y. Liu, J. Gu, Z. Y. Ma, J. J. Zha, B. Dahal, L.-N. Zhang, A. N. Chishti, L. B. Ni, G. W. Diao, Y. G. Wei, *Adv. Funct. Mater.* **2021**, *31*, 2106147.
[13] R. Zhang, Z. H. Wei, G. Y. Ye, G. J. Chen, J. J. Miao, X. H. Zhou, X. W. Zhu, X. Q. Cao, X. N. Sun, *Adv. Energy Mater.* **2021**, *11*, 2101758.
[14] X. Wang, F. Li, W. Z. Li, W. B. Gao, Y. Tang, R. Li, *J. Mater. Chem. A* **2017**, *5*, 17982.
[15] Z.-Y. Yu, Y. Duan, X.-Y. Feng, X. X. Yu, M.-R. Gao, S.-H. Yu, *Adv. Mater.* **2021**, *33*, 2007100.
[16] N. K. Oh, J. Seo, S. J. Lee, H.-J. Kim, U. Kim, J. Lee, Y.-K. Han, H. Park, *Nat. Commun.* **2021**, *12*, 4606.
[17] C. Tang, N. Y. Cheng, Z. H. Pu, W. Xing, X. P. Sun, *Angew. Chem., Int. Ed.* **2015**, *54*, 9351.
[18] H. Q. Zhou, F. Yu, Y. F. Huang, J. Y. Sun, Z. Zhu, R. J. Nielsen, R. He, J. M. Bao, W. A. Goddard, S. Chen, Z. F. Ren, *Nat. Commun.* **2016**, *7*, 12765.
[19] Y. C. Fan, J. R. Wang, M. W. Zhao, *Nanoscale* **2019**, *11*, 14836.
[20] G. Q. Zhao, K. Rui, S. X. Dou, W. P. Sun, *Adv. Funct. Mater.* **2018**, *28*, 1803291.
[21] H. Q. Wang, X. Q. Wang, B. J. Zheng, D. X. Yang, W. L. Zhang, Y. F. Chen, *Electrochim. Acta* **2019**, *318*, 449.
[22] H. Y. Yang, P. F. Guo, R. R. Wang, Z. L. Chen, H. B. Xu, H. G. Pan, D. L. Sun, F. Fang, R. B. Wu, *Adv. Mater.* **2022**, 2107548.
[23] Y. Wei, C. H. Shin, E. B. Tetteh, B. J. Lee, J. S. Yu, *ACS Appl. Energy Mater.* **2020**, *3*, 822.
[24] Y. Xu, X. J. Chai, T. L. Ren, H. J. Yu, S. L. Yin, Z. Q. Wang, X. N. Li, L. Wang, H. J. Wang, *Chem. - Eur. J.* **2019**, *25*, 16074.
[25] X. Y. Shan, J. Liu, H. R. Mu, Y. Xiao, B. B. Mei, W. G. Liu, G. Lin, Z. Jiang, L. P. Wen, L. Jiang, *Angew. Chem., Int. Ed.* **2020**, *59*, 1659.
[26] J. Jian, W. Chen, D. C. Zeng, L. M. Chang, R. Zhang, M. C. Jiang, G. T. Yu, X. R. Huang, H. M. Yuan, S. H. Feng, *J. Mater. Chem. A* **2021**, *9*, 7586.
[27] X. J. Feng, L. Feng, M. H. Jin, J. Zhai, L. Jiang, D. B. Zhu, *J. Am. Chem. Soc.* **2004**, *126*, 62.
[28] W. K. Pei, J. Y. Zhang, H. J. Tong, M. N. Ding, F. Y. Shi, R. Z. Wang, Y. N. Huo, H. X. Li, *Appl. Catal., B* **2021**, *282*, 119575.
[29] L. Zhang, A. P. Wu, M. Tian, Y. L. Xiao, X. Shi, H. J. Yan, C. G. Tian, H. G. Fu, *Chem. Commun.* **2018**, *54*, 11088.
[30] A. Banerjee, S. Bhatnagar, K. K. Upadhyay, P. Yadav, S. Ogale, *ACS Appl. Mater. Interfaces* **2014**, *6*, 18844.
[31] S. Riyajuddin, K. Azmi, M. Pahuja, S. Kumar, T. Maruyama, C. Bera, K. Ghosh, *ACS Nano* **2021**, *15*, 5586.
[32] Y. Gu, A. P. Wu, Y. Q. Jiao, H. R. Zheng, X. Q. Wang, Y. Xie, L. Wang, C. G. Tian, H. G. Fu, *Angew. Chem., Int. Ed.* **2021**, *60*, 6673.
[33] A. P. Wu, Y. Xie, H. Ma, C. G. Tian, Y. Gu, H. J. Yan, X. M. Zhang, G. Y. Yang, H. G. Fu, *Nano Energy* **2018**, *44*, 353.
[34] J. Wang, F. Xu, H. Y. Jin, Y. Q. Chen, Y. Wang, *Adv. Mater.* **2017**, *29*, 1605838.
[35] H. J. Yan, C. G. Tian, L. Wang, A. P. Wu, M. C. Meng, L. Zhao, H. G. Fu, *Angew. Chem., Int. Ed.* **2015**, *54*, 6325.
[36] J. H. Lin, H. H. Wang, J. Cao, F. He, J. C. Feng, J. L. Qi, *J. Colloid Interface Sci.* **2020**, *571*, 260.
[37] Y. Z. Li, Z. Wang, J. Hu, S. W. Li, Y. C. Du, X. J. Han, P. Xu, *Adv. Funct. Mater.* **2020**, *30*, 1910498.
[38] Y. Wang, X. P. Li, M. M. Zhang, Y. G. Zhou, D. W. Rao, C. Zhong, J. F. Zhang, X. P. Han, W. B. Hu, Y. C. Zhang, K. Zaghib, Y. S. Wang, Y. D. Deng, *Adv. Mater.* **2020**, *32*, 2000231.
[39] X. Y. Li, L. P. Xiao, L. Zhou, Q. C. Xu, J. Weng, J. Xu, B. Liu, *Angew. Chem., Int. Ed.* **2020**, *59*, 21106.
[40] R. Gond, D. K. Singh, M. Eswaramoorthy, P. Barpanda, *Angew. Chem., Int. Ed.* **2019**, *58*, 8330.
[41] L. T. Yan, Y. L. Xu, P. Chen, S. Zhang, H. M. Jiang, L. Z. Yang, Y. Wang, L. Zhang, J. X. Shen, X. B. Zhao, L. Z. Wang, *Adv. Mater.* **2020**, *32*, 2003313.
[42] Z. Zhang, X. P. Li, C. Zhong, N. Q. Zhao, Y. D. Deng, X. P. Han, W. B. Hu, *Angew. Chem., Int. Ed.* **2020**, *59*, 7245.
[43] C. L. Hu, L. Zhang, Z. J. Zhao, A. Li, X. X. Chang, J. L. Gong, *Adv. Mater.* **2018**, *30*, 1705538.
[44] B. Liu, Y. Wang, H. Q. Peng, R. O. Yang, Z. Jiang, X. T. Zhou, C. S. Lee, H. J. Zhao, W. J. Zhang, *Adv. Mater.* **2018**, *30*, 1803144.
[45] L. L. Huang, D. W. Chen, G. Luo, Y. R. Lu, C. Chen, Y. Q. Zou, C. L. Dong, Y. F. Li, S. Y. Wang, *Adv. Mater.* **2019**, *31*, 1901439.
[46] Y. Pan, K. A. Sun, S. J. Liu, X. Cao, K. L. Wu, W. C. Cheong, Z. Chen, Y. Wang, Y. Li, Y. Q. Liu, D. S. Wang, Q. Peng, C. Chen, Y. D. Li, *J. Am. Chem. Soc.* **2018**, *140*, 2610.
[47] T. Ouyang, Y. Q. Ye, C. Y. Wu, K. Xiao, Z. Q. Liu, *Angew. Chem., Int. Ed.* **2019**, *58*, 4923.
[48] T. Tang, W. J. Jiang, S. Niu, N. Liu, H. Luo, Y. Y. Chen, S. F. Jin, F. Gao, L. J. Wan, J. S. Hu, *J. Am. Chem. Soc.* **2017**, *139*, 8320.
[49] Y. S. Du, G. Z. Cheng, W. Luo, *Nanoscale* **2017**, *9*, 6821.
[50] Y. X. Huang, Z. H. Wang, Y. Jiang, S. J. Li, Z. H. Li, H. Q. Zhang, F. Wu, M. Xie, L. Li, R. J. Chen, *Nano Energy* **2018**, *53*, 524.
[51] G. C. Yang, Y. Q. Jiao, H. J. Yan, Y. Xie, A. P. Wu, X. Dong, D. Z. Guo, C. G. Tian, H. G. Fu, *Adv. Mater.* **2020**, *32*, 2000455.
[52] H. J. Yan, Y. Xie, A. P. Wu, Z. C. Cai, L. Wang, C. G. Tian, X. M. Zhang, H. G. Fu, *Adv. Mater.* **2019**, *31*, 1901174.
[53] A. P. Wu, Y. Gu, B. R. Yang, H. Wu, H. J. Yan, Y. Q. Jiao, D. X. Wang, C. G. Tian, H. G. Fu, *J. Mater. Chem. A* **2020**, *8*, 22938.
[54] G. Chen, Y. P. Zhu, H. M. Chen, Z. W. Hu, S. F. Hung, N. N. Ma, J. Dai, H. J. Lin, C. T. Chen, W. Zhou, Z. P. Shao, *Adv. Mater.* **2019**, *31*, 1900883.
[55] J. H. Zhang, Q. C. Xu, Y. J. Hu, H. Jiang, C. Z. Li, *Chem. Commun.* **2020**, *56*, 14451.
[56] Z.-P. Wu, H. B. Zhang, S. W. Zuo, Y. Wang, S. L. Zhang, J. Zhang, S.-Q. Zang, X. W. Lou, *Adv. Mater.* **2021**, *33*, 2103004.
[57] X. Xu, F. Song, X. L. Hu, *Nat. Commun.* **2016**, *7*, 12324.
[58] M. Wang, L. Zhang, Y. J. He, H. W. Zhu, *J. Mater. Chem. A* **2021**, *9*, 5320.
[59] R. Wang, K. Hashimoto, A. Fujishima, M. Chikuni, E. Kojima, A. Kitamura, M. Shimohigoshi, T. Watanabe, *Nature* **1997**, *388*, 431.
[60] P. L. Zhai, Y. X. Zhang, Y. Z. Wu, J. F. Gao, B. Zhang, S. Y. Cao, Y. T. Zhang, Z. W. Li, L. C. Sun, J. G. Hou, *Nat. Commun.* **2020**, *11*, 5462.
[61] L. B. Wu, L. Yu, F. H. Zhang, B. McElhenny, D. Luo, A. Karim, S. Chen, Z. F. Ren, *Adv. Funct. Mater.* **2020**, *31*, 2006484.
[62] T. Meng, J. W. Qin, S. G. Wang, D. Zhao, B. G. Mao, M. H. Cao, *J. Mater. Chem. A* **2017**, *5*, 7001.